GDCh Research Article Angewandte International Edition Chemie www.angewandte.org

How to cite: *Angew. Chem. Int. Ed.* **2024**, *63*, e202405307
doi.org/10.1002/anie.202405307

ZIF Glasses Hot Paper

Insights Into the Mechanochemical Glass Formation of Zeolitic Imidazolate Frameworks

*Wen-Long Xue, Chinmoy Das, Jan-Benedikt Weiß, and Sebastian Henke**

Abstract: Metal–organic framework (MOF) glasses, known for their potential in gas separation, optics, and solid-state electrolytes, benefit from the processability of their (supercooled) liquid state. Traditionally, MOF glasses are produced by heating MOF crystals to their melting point and then cooling the liquid MOF to room temperature under an inert atmosphere. While effective, this melt-quenching technique requires high energy due to the high temperatures involved. It also limits the scope of new material development by restricting the compositional range to only those combinations of metal ions and linkers that are highly thermally stable. An alternative, mechanical milling at room temperature, has demonstrated its capability to transform MOF crystals into amorphous phases. However, the specific conditions under which these amorphous phases exhibit glass-like behavior remain uncharted. In this study, we explore the mechanochemical amorphization and vitrification of a variety of zeolitic imidazolate frameworks (ZIFs) with diverse linkers and different metal ions (Zn^{2+}, Co^{2+} and Cu^{2+}) at room temperature. Our findings demonstrate that ZIFs capable of melting can be successfully converted into glasses through ball-milling. Remarkably, some non-meltable ZIFs can also be vitrified using the ball-milling technique, as highlighted by the preparation of the first Cu^{2+}-based ZIF glass.

Introduction

Metal–organic frameworks (MOFs) are hybrid materials composed of metal ions and organic ligands interconnected to a continuous network.[1] At present, nearly 100,000 crystalline MOFs have been reported in the literature,[2] and many of them exhibit great potential for applications in various fields. Besides the omnipresent crystalline MOFs, liquid[3] and glassy MOFs,[4–5] categorized as the fourth-generation of coordination polymers (CPs),[6] are an emerging area. Recently, the interest in glass materials has grown rapidly due to the corresponding advantages in processing and shaping these materials. The advanced processability and grain-boundary-free nature of isotropic liquid and glassy MOF phases compared to their crystalline relatives opens new routes for applications ranging from gas separation[7] to solid-state ionics.[8–9] Moreover, MOF glasses have been proposed as attractive materials for utilization as phosphors[10] and in radioactive waste storage.[11]

The family of zeolitic imidazolate frameworks (ZIFs) represents the most investigated subset of meltable and glass-forming MOFs. ZIFs are based on tetrahedrally coordinated transition metal ions (e.g. Zn^{2+} or Co^{2+}), which are linked by imidazolate linkers creating a typically three-dimensional network.[12] Interestingly, among the plethora of MOFs, just a few ZIFs transform into stable liquids when heated under an inert atmosphere before they undergo thermal decomposition.[4,13] During melting, the metal-linker bonds are dynamically broken and reformed, giving rise to ZIF liquids.[3] When the ZIF liquids are cooled down, they vitrify, forming melt-quenched glasses (MQGs).[14] Practically, melting a ZIF requires relatively high temperatures (usually $>400\,°C$) and thus a significant energy consumption.[4] Moreover, the necessity to obtain ZIF glasses via the liquid ZIF phase, drastically limits the choice of ZIF glass former, as many of the functional groups utilized in substituted imidazolate linkers are sensitive to high temperature (e.g. halide substituents or nitro groups[12,15]). The prototypical glass former ZIF-4, for example, requires a very high melting temperature of $590\,°C$,[3,16] resulting in a partially decomposed MQG.[4,17]

Ball-milling is an established technique for synthesizing microcrystalline MOF powders. In this method, typically, a metal oxide is milled in a vibratory mixer mill alongside the organic linker in its acid form in the presence of a small quantity of additives and templating solvent molecules.[18–20] Conversely, post-synthetic ball-milling (PSBM) of MOF microcrystals, conducted without solvent, leads to the rapid amorphization of the materials. The mechanical impact during PSBM aids in breaking and reforming coordination bonds, ultimately resulting in the formation of amorphous

[*] W.-L. Xue, Dr. C. Das, J.-B. Weiß, Prof. Dr. S. Henke
Anorganische Chemie, Fakultät für Chemie und Chemische Biologie
Technische Universität Dortmund
Otto-Hahn Straße 6, 44227 Dortmund, Germany
E-mail: sebastian.henke@tu-dortmund.de

Dr. C. Das
Department of Chemistry
SRM University-AP
Andhra Pradesh-522240, India

solids.[21] For a variety of dense coordination polymers (CPs) and networks (CNs) based on triazolate, dicyanamide, or cyanide linkers the amorphous phases obtained by PSBM were shown to exhibit a glass transition.[22–23] For ZIFs, different methods of mechanical perturbation[24] were shown to have a facilitative effect on ZIF melting and glass formation. Applying high hydrostatic pressure[25] or high-frequency vibration,[26] for example, promotes ZIF melting (i.e. dynamic metal-linker bond breaking). Previous research has shown that PSBM can cause rapid amorphization of crystalline ZIFs, including ZIF-4 ($Zn(im)_2$; **cag** topology; im^- = imidazolate), ZIF-zni ($Zn(im)_2$; **zni** topology) and ZIF-8 ($Zn(mim)_2$; **sod** topology; mim^- = 2-methylimidazolate).[27–30] However, it is unclear whether the amorphized ZIFs exhibit glassy behavior. Recently, a mechanochemical synthesis by ball-milling has been employed to prepare ZIF-62 ($Zn(im)_{2-x}(bim)_x$; **cag** topology when crystalline; bim^- = benzimidazolate) by reaction of ZnO with imidazole and benzimidazole in the presence of small amounts of *N,N*-dimethylformamide (DMF).[31–32] Depending on the composition of the reaction mixture, the derived material was either crystalline (for $0.05 \le x \le 0.30$) or amorphous (for $0.35 \le x \le 1$).[33] Interestingly, the amorphous ZIF-62 prepared by ball-milling showed a calorimetric glass transition, showcasing that glassy ZIF-62 can be prepared mechanochemically at room temperature by increasing the bim^- concentration in the ball-milling synthesis. However, the technique of preparing a ZIF-62 glass by ball-milling via a considerable increase in the bulky linker fraction (i.e. $0.35 \le x(bim^-) \le 1$) has constraints, such as the possibility of porosity blockage in the glasses and a significant rise of the glass transition temperature (T_g), necessitating a higher processing or working temperature.

While ball-milling is commonly employed for the synthesis of crystalline ZIFs or their transformation into amorphous states, its capacity for enabling direct vitrification of ZIFs at room temperature remains uncharted. Herein, we report a detailed study of the utility of solvent-free PSBM for the vitrification of crystalline ZIFs of varying chemical composition, network topology and porosity at ambient temperatures (Figure 1). To evaluate the potential of PSBM for ZIF glass formation, we investigate several meltable and glass-forming ZIFs,[17,34–35] namely ZIF-4(Zn/Co), ZIF-zni(Zn/Co), ZIF-62(Zn/Co), ZIF-UC-5 and TIF-4, but also ZIFs known not to melt when in pure form, i.e. ZIF-76[36] and ZIF-8,[4,37] and ZIFs which were previously not studied in terms of glass formation, i.e. ZIF-70[12] and ZIF-Cu-1 ($Cu(im)_2$)[38] (Figure 2). These materials comprise representatives with Zn^{2+} and Co^{2+} tetrahedral building units typical for ZIFs, as well as a Cu^{2+}-based ZIF featuring drastically flattened pseudo-tetrahedral units. It is important to note that Cu^{2+}-based ZIFs have not been studied in terms of melting and glass formation so far. X-ray powder diffraction (XRPD), differential scanning calorimetry (DSC), simultaneous thermogravimetric and differential thermal analyses (TG/DTA), X-ray total scattering and its deduced pair distribution functions (PDFs), scanning electron microscopy (SEM), and CO_2 gas sorption measurements provide important insights into the thermal, structural, and textural features of the ZIFs after varying PSBM times (between 5 and 60 min). We find that PSBM transforms several of these ZIFs into glasses (MIGs = milling-induced glasses), highlighted by the preparation of the first ZIF glass with Cu^{2+} building units, while other ZIFs amorphize but show no glassy behavior. Our results provide a first guide for preparing ZIF glasses by mechanical milling at ambient temperature but also expose some limitations of the method.

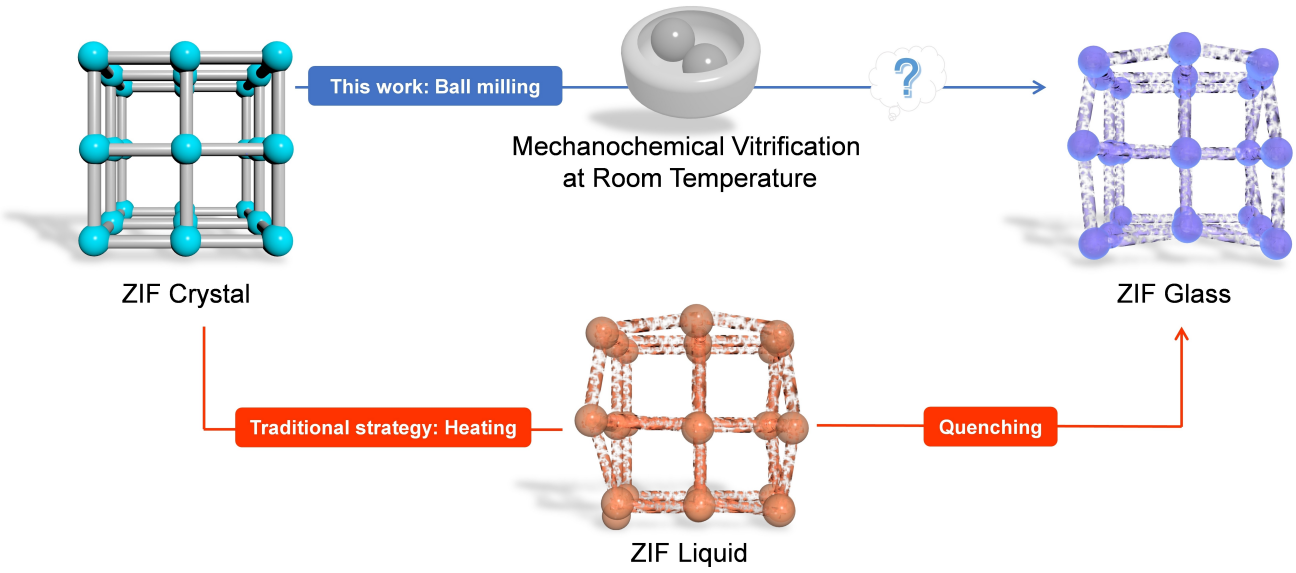

Figure 1. Schematic representation of the traditional route to ZIF glass formation (red line) and the mechanochemical vitrification approach followed in this work (blue line).

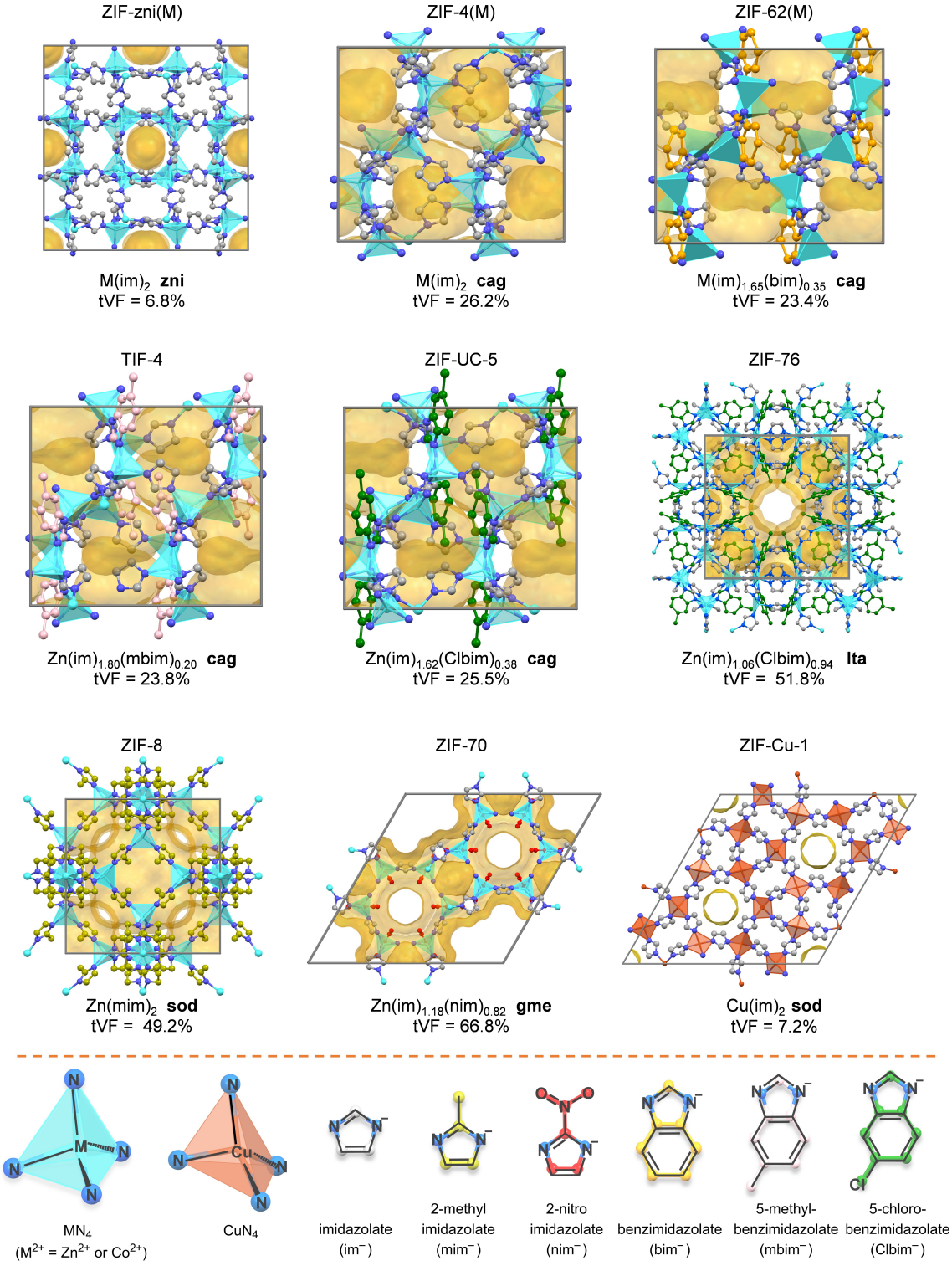

Figure 2. Crystal structures (top) and building units (bottom) of the ZIFs investigated in this work. ZIF-zni (CCDC code IMIDZB) viewed along the crystallographic *c* axis, ZIF-4 (CCDC code IMIDZB11), ZIF-62 (CCDC code SIWJAM), TIF-4 (CCDC code QOSYAZ) and ZIF-UC-5 (CCDC code GULVIV) viewed along the crystallographic *b* axis. ZIF-76 (CCDC code GITWEM) and ZIF-8 (CCDC code FAWCEN03) viewed along the crystallographic *a* axis. ZIF-70 (CCDC code GITVEL) and ZIF-Cu-1 (CCDC code CUIMDZ01) viewed along the crystallographic *c* axis. Hydrogen atoms are omitted for clarity. The theoretical void fractions (tVFs) were calculated using Mercury software with a probe radius of 1.6 Å and a grid spacing of 0.2 Å and are shown in pale yellow. Solvent molecules were removed and linker disorder was resolved as far as possible without changing the space group symmetry before the calculation of the tVFs. If H atoms were not included in the reported crystal structures, they were positioned at geometrical positions before the calculation of the tVF. The compositions of the ZIFs were obtained by ^{1}H NMR spectroscopy of acid-digested samples.

Results and Discussion

Crystalline ZIF Synthesis and Structural Characterization

Twelve different ZIF crystals were synthesized by adapting established solvothermal reaction procedures (see Supporting Information Section 1).[12,36, 38–39] Among these ZIF-4(M), ZIF-zni(M) and ZIF-62(M) were prepared using either Zn^{2+} or Co^{2+} as metal centers (M^{2+}), whereas TIF-4, ZIF-UC-5, ZIF-76, ZIF-8 and ZIF-70 avail Zn^{2+} as inorganic building unit, and ZIF-Cu-1 was prepared with Cu^{2+} as the metal center (Figure 2). The ZIFs comprise a variety of functionalized linkers as well as network topologies of diverse porosities. The theoretical void fractions (tVFs) of the ZIFs calculated based on reported crystal structures range from about 7 % (ZIF-zni and ZIF-Cu-1) up to about 67 % (ZIF-70). After washing and solvent exchange procedures, the desolvated Zn- and Co-ZIF materials were obtained by heating to 170 °C under a dynamic vacuum for 6 h, while ZIF-Cu-1 was activated at 110 °C because of its lower decomposition temperature. The identity and purity of the crystalline ZIFs were verified by structureless profile fits (Pawley method) of XRPD patterns using reference data from the literature (Figures S1–12, Table S3). All compounds are phase-pure except for ZIF-UC-5, which contained about 5 wt % of ZIF-76 as a parasitic phase according to a dual-phase Rietveld refinement of the XRPD pattern (Figure S7). The latter sample is therefore referred to as ZIF-76/UC-5. Complete removal of solvents from the pores of the ZIFs is demonstrated by ^{1}H nuclear magnetic resonance (^{1}H NMR) and Fourier-transform infrared (FTIR) spectroscopy data (see Supporting Information Section 3–4). ^{1}H NMR spectroscopy of acid-digested samples was performed to determine the linker ratios of the mixed-linker materials ZIF-62(M), TIF-4, ZIF-70, ZIF-76 and ZIF-76/UC-5, leading to the chemical compositions given in Figure 2 (Figures S35–36 and S41–44).

Amorphization by Post-Synthetic Ball Milling

The activated microcrystalline ZIFs were treated with PSBM at 25 Hz in a vibratory shaker mill for 5, 10, and 15 minutes, respectively, using a 10 mL stainless steel grinding jar with two 8 mm stainless-steel balls and ca. 50 mg ZIF. The derived PSBM materials are denoted by ZIF-*X*-5min/10min/15min according to the corresponding PSBM time. Additional 30 min and 60 min ball milled samples were prepared for ZIF-8 (ZIF-8-30min and ZIF-8-60min). The XRPD patterns of almost all ball-milled ZIFs show only diffuse scattering without sharp Bragg reflections already after 5 min of PSBM proving rapid amorphization of the materials (Figures 3 and S14–20). The only exceptions are the ZIF-zni(M) samples, which still contain reflections assigned to the crystalline ZIF-zni phase after 5 min PSBM, even though the reflections are of diminished intensity and increased peak width (Figures 3 and S16). Upon increasing the PSBM times, the Bragg reflections of the ZIF-zni phases

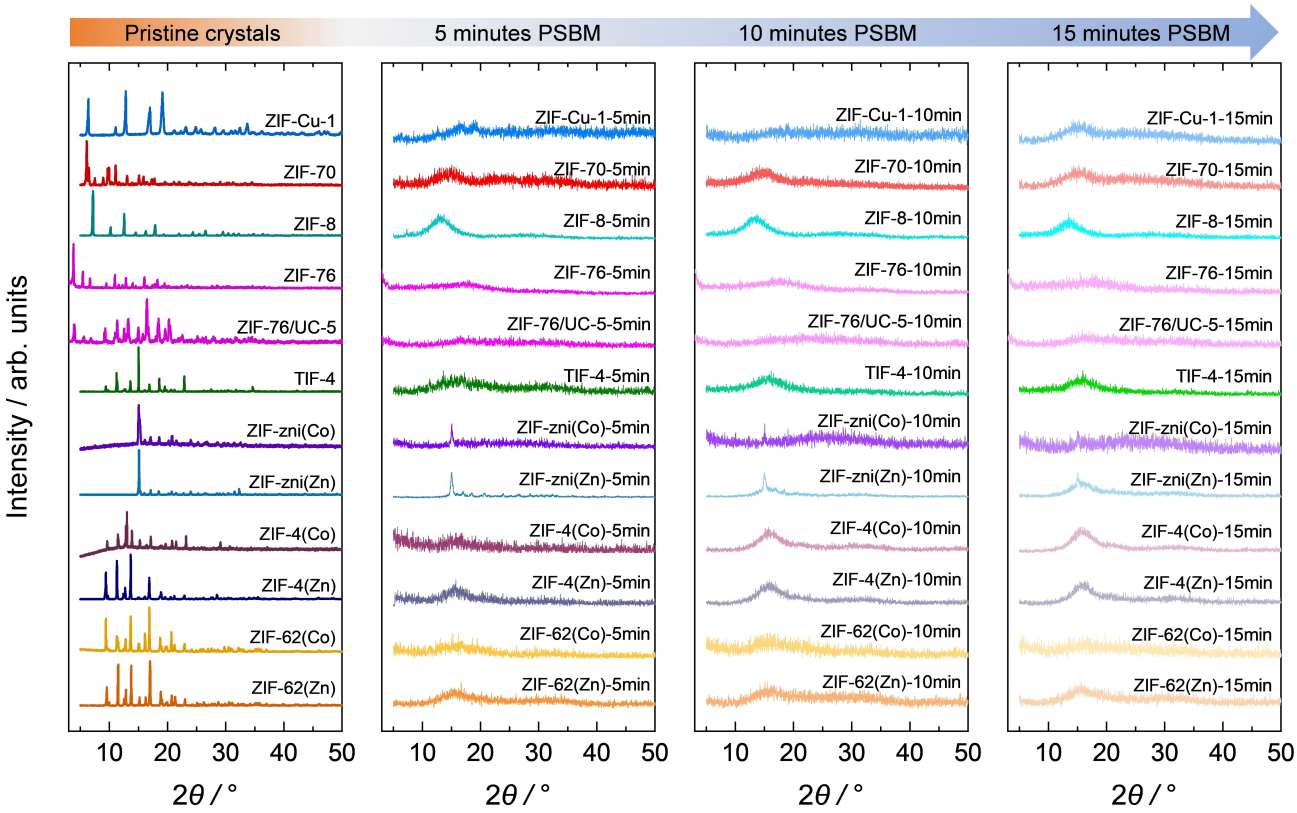

Figure 3. XRPD patterns of the pristine ZIF polycrystalline materials and after 5, 10 and 15 min PSBM.

decrease further in intensity, but the samples are still not fully amorphized after 15 min PSBM. The residual crystallinity of the ZIF-zni(Zn) samples was estimated from profile fitting of the XRPD data (Figures S21–24). It is observed that within the first 10 min PSBM, the degree of crystallinity of the sample gradually reduces to 49 %, while after 15 min PSBM, a degree of crystallinity of 36 % remains. The higher resistance of ZIF-zni towards amorphization by PSBM can be explained by the higher density of ZIF-zni ($\rho = 1.56\ g\,cm^{-3}$)[40] compared to the other Zn- and Co-based ZIFs studied here ($0.78\ g\,cm^{-3} \le \rho \le 1.32\ g\,cm^{-3}$),[17] as it is known that a higher density correlates well with increased elastic moduli and hardness.[41]

In agreement with previous structural investigations of amorphized ZIFs,[27,42] PDFs derived from X-ray total scattering data of selected pristine and 5-min-ball-milled ZIF samples show that the short-range structure (< 6 Å) of the crystalline phase (i.e., metal ions surrounded by four imidazolate-based linkers) is preserved in the amorphous PSBM samples (Figures S30–34). Hence, the PDFs of the amorphous PSBM-derived ZIFs are largely identical to those of the literature-known ZIF MQGs. In line with the loss of long-range order, increased structural heterogeneity and distortions in the ball-milled ZIFs are evident from the broadening of various vibrational bands in the FTIR spectra relative to the bands of the crystalline parent materials (Figures S47–58). In particular, the asymmetric stretching vibrational bands of the MN_4 polyhedra (M^{2+}=Zn^{2+}, Co^{2+}, Cu^{2+}) located at 300 cm^{-1} in the far-IR spectra exhibit notably broader profiles in the PSBM samples compared to their crystalline counterparts, observable as early as 5 minutes into the ball-milling process. These bands mirror the widths seen in the corresponding MN_4 vibrations of MQG reference samples (Figures S59–67 and Table S4). An exception is again observed with ZIF-zni(Zn), which shows a gradual broadening over the course of PSBM, consistent with the gradual decline in crystallinity discussed above. SEM images reveal that the solvothermally synthesized ZIFs, initially characterized by large crystals (up to several hundred micrometers in size), undergo significant fragmentation into smaller particles ranging from 1 to 10 µm in size following a 5-min PSBM treatment (Figures S106–108 and Table S10). Prolonged ball-milling times result in only marginal further reductions in particle size.

CO_2 Physisorption Data and Porosity Analysis

Since it is established that N_2 is hardly adsorbed at 77 K in some of the ZIFs studied here,[13,17,43] the evolution of the ZIFs' porosity with PSBM time was studied by isothermal CO_2 sorption at 195 K (Figures S68–75 and Table S5). CO_2 has a smaller kinetic diameter than N_2 and can enter very narrow micropores.[17] The maximum gas pressure used for the data collection is 95 kPa, corresponding to a relative pressure p/p_0 of about 0.50, ensuring the complete filling of the materials' micropores. The maximum adsorbed gas capacities at 95 kPa (V_{ads}^{max}) of CO_2 of all studied ZIFs progressively decrease with increasing PSBM time except for ZIF-zni(Zn) (Figure 4a). The reduced CO_2 capacities indicate that the materials densify during the PSBM-induced amorphization. As expected, the rate of densification decreases with increasing ball-milling-time, indicating that the most significant structural changes under amorphization appear during the first few minutes of milling. The more porous ZIFs (i.e., ZIF-4(M), ZIF-8 and ZIF-76) undergo stronger densification (stronger loss of porosity) with increased ball-milling time than the less porous ZIF-62(M) (Figure 4b). This is in accordance with the larger bulk moduli and increased mechanical resistance of ZIF-62(M) compared to the isoreticular but more porous ZIF-4(M).[44] Surprisingly, the porosity of ZIF-zni(Zn) increases with PSBM. V_{ads}^{max} progressively reaches 181 % of the capacity of pristine ZIF after 10 min of PSBM and then settles at 171 % of the original capacity after 15 min of PSBM. This unusual behavior likely is because the **zni** topology is one of the densest ZIF topologies known, and the increase in its disorder by PSBM leads to an increase in its porosity.[45]

Except for ZIF-8 and ZIF-Cu-1, the CO_2 capacity is very similar for the samples treated with 15 min PSBM, signifying that they all form amorphous MOFs of similar porosity and density. Notably, the CO_2 capacities at 95 kPa are in the range from 50 to 65 $cm^3\,g^{-1}$ (STP), which is very similar to the CO_2 capacity of the MQGs of ZIF-4, ZIF-62 and TIF-4 determined under the same conditions.[17] ZIF-8 is more resistant to a framework collapse than the other ZIFs, so a substantially higher porosity is observed after 15 min of PSBM ($V_{ads}^{max} = 82\ cm^3\,g^{-1}$). Even after 60 min of PSBM, the amorphized ZIF-8 has a substantially higher sorption capacity than the other ZIFs subjected to only 15 min PSBM ($V_{ads}^{max} = 70\ cm^3\,g^{-1}$). We speculate that the methyl groups present at position 2 of the mim^- linker might be the reason for the formation of a more open amorphous network structure in the case of ball-milled ZIF-8 compared to the other ZIFs, which use linkers that are not substituted at position 2.[43]

ZIF-Cu-1 is very different to all the other materials investigated here. As expected from its low tVF, the gravimetric CO_2 capacity ($V_{ads}^{max} = 25\ cm^3\,g^{-1}$ (STP)) of the crystalline ZIF-Cu-1 is on the same scale as the capacity of crystalline ZIF-zni ($V_{ads}^{max} = 31\ cm^3\,g^{-1}$ (STP)). In contrast to

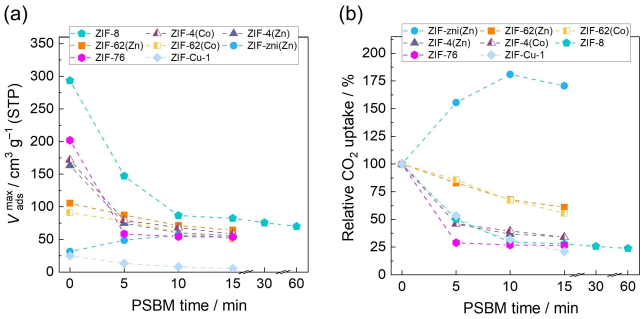

Figure 4. (a) Absolute CO_2 uptake (V_{ads}^{max}) recorded at 195 K, 95 kPa and (b) the corresponding relative CO_2 uptake ($V_{ads}^{max}(t)/V_{ads}^{max}(t=0)$) as a function of PSBM time of the studied ZIF samples. The lines are just a guide to the eyes.

ZIF-zni(Zn), milling does not increase the porosity of ZIF-Cu-1 but progressively densifies the material so that V_{ads}^{max} amounts to only about 5 $cm^3 g^{-1}$ (STP) after 15 min PSBM, rendering the amorphous ZIF-Cu-1-15min essentially non-porous. Since the dense ZIF-zni(Zn) and ZIF-Cu-1 both contain the same im^- linkers, the drastic difference in milling-induced structural evolution between these two materials may be ascribed to their inorganic building units. The almost perfectly tetrahedral Zn^{2+} centers of ZIF-zni(Zn) (geometry index $\tau_4 = 0.97$ and 0.95 for the two crystallographically independent Zn^{2+} ions; $\tau_4 = 1$ for tetrahedral and $\tau_4 = 0$ for square planar[46]) seem to facilitate a looser packing of the building units in the amorphous frameworks compared to the severely flattened pseudo-tetrahedron of Cu^{2+} in ZIF-Cu-1 ($\tau_4 = 0.47$; Figure 5).

Thermal Properties

To examine the thermal stability and possible phase/glass transitions of the pristine ZIFs and the corresponding PSBM samples, simultaneous thermogravimetric and differential thermal analyses (TG/DTA) were carried out between 40 and 800 °C under N_2 atmosphere (Figures S76–87). The decomposition temperature (T_d) of all ZIFs generally decreases slightly with increasing PSBM time (Table S8). The reduced thermal stability may be due to increased defect concentrations and unfavorable structural distortions caused by PSBM.

To screen the samples for thermal phase changes, additional cyclic DSC experiments (two upscans, one downscan) were performed between ambient temperature and T_d also under N_2 atmosphere (Figures 6, S88–91 and S99). Excitingly, the ZIFs which are known glass formers (ZIF-62(M), ZIF-4(M), ZIF-zni(Zn), ZIF-76/UC-5 and TIF-4) exhibit a well-defined glass transition signal in the first upscan of the DSC already after only 5 minutes of PSBM (Figures 6 and S88). Hence, these PSBM-amorphized materials represent ZIF MIGs that transition to a supercooled liquid upon heating.[47] This proves that the vitrification of these compounds can be achieved by ball milling at room temperature instead of heating across the materials' melting points, followed by melt-quenching. We believe that the mechanical energy generated by compression and shear, together with potential instantaneous temperature hotspots, achieves the glass transition process through PSBM.[48–49] Notably, the T_g values of the MIGs are lower than the T_g values of the corresponding glasses prepared by conventional melt-quenching methods (MQGs). Interestingly, the T_g values of the MIGs decrease further with increasing PSBM time, which can be rationalized by an increasing number of structural defects (i.e. undercoordinated Zn^{2+} ions, linkers with dangling bonds) with longer milling times (Figures 6 and S88).[22,50] The lower T_g values of the MIGs imply that these glasses could be molded and shaped at a lower temperature than the corresponding MQGs. Moreover, the MIGs transform into the supercooled liquid state at T_g, while the MQGs must first be obtained by heating the crystalline precursors to the higher T_m.

In the second DSC upscan of the MIGs, the T_g values converge to the values known for the corresponding MQGs. This is likely because most of the structural defects arising from PSBM are healed by thermal relaxation in the supercooled liquid state. Broad exothermic features in the DSC traces of the first upscans of the PSBM samples of ZIF-62(Zn) at temperatures between 400 °C and 500 °C support this reasoning.

The DSC data of both ZIF-4(Zn/Co) and ZIF-zni(Zn/Co) reveal distinct thermal characteristics (Figure 6b and c). Similar to crystalline ZIF-4(Zn), which recrystallizes to ZIF-zni(Zn) after thermal amorphization, the MIGs ZIF-4(Zn)-5min, -10min and -15min also recrystallize to the ZIF-zni(Zn) polymorph after passing through their glass transition (confirmed by variable temperature XRPD, Figures S27–29). Interestingly, the recrystallization temperature (T_{rc}) and the corresponding enthalpy (ΔH_{rc}) decrease slightly with increased milling time (Tables S8–S9). The PSBM samples derived from ZIF-zni(Zn) also recrystallize to the same phase after passing through the glass transition; however, here, T_{rc} and ΔH_{rc} increase with milling time. These thermal variations align with the milling-induced changes in the porosity and density, where ZIF-zni(Zn) experiences an increase in porosity and a decrease in density with milling, while ZIF-4(Zn) shows the opposite trend. Additionally, ZIF-zni(Zn) does not fully amorphize even after 15 min of PSBM. Consequently, the remaining crystalline grains of the ZIF-zni phase in the ball-milled materials aid in recrystallization, as they serve as nucleation sites for crystal growth when subjected to elevated temperatures.

It can generally be stated that ΔH_{rc} for all ball-milled ZIF-4(Zn) and ZIF-zni(Zn) materials ($\Delta H_{rc} = -7.2$ to -10.2 kJ mol^{-1}) is slightly smaller than that of pristine ZIF-4(Zn) ($\Delta H_{rc} = -10.6$ kJ mol^{-1}). This finding indicates incomplete recrystallisation in the PSBM samples so that a substantial proportion of the amorphous phase remains. This hypothesis is reinforced by the observation that the melting enthalpy (ΔH_m) of the recrystallized ZIF-zni(Zn) phases from the PSBM materials ($\Delta H_m = 5.0$ to 7.7 kJ mol^{-1})

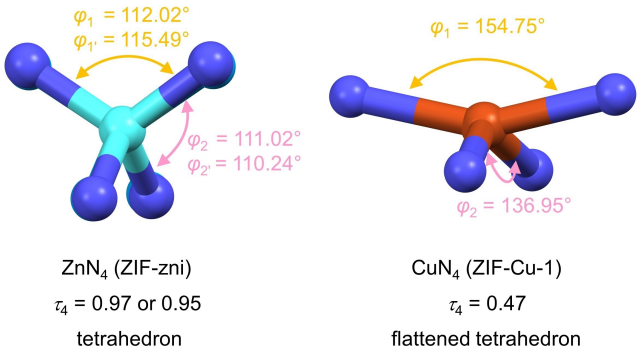

Figure 5. Coordination environments of Zn^{2+} in ZIF-zni (left, CCDC code IMIDZB) and Cu^{2+} in ZIF-Cu-1 (right, CCDC code CUIMDZ01). The two largest N–M–N angles (φ_1 and φ_2) utilized to calculate the geometry index (τ_4) are shown in both diagrams. Note, ZIF-zni has two crystallographically independent Zn^{2+} ions exhibiting slightly different angles.

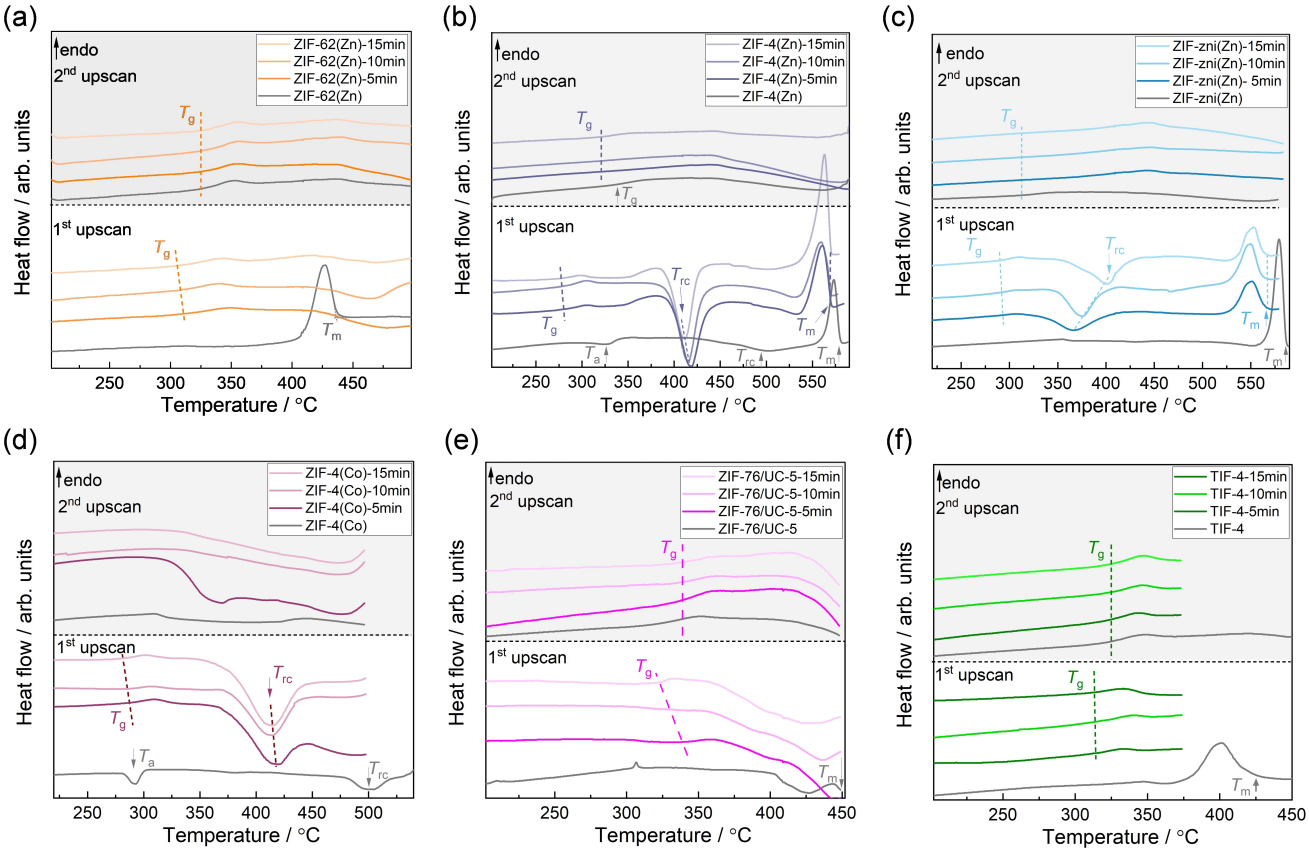

Figure 6. First and second upscans of DSC measurements of (a) ZIF-62(Zn), (b) ZIF-4(Zn), (c) ZIF-zni(Zn), (d) ZIF-4(Co), (e) ZIF-76/UC-5, (f) TIF-4, and the corresponding samples after 5, 10 and 15 min PSBM. The heating rate for all measurements was +10 °C min^{-1}. The colored arrows and dotted lines indicate the amorphization temperature (T_a), glass transition temperature (T_g), recrystallization temperature (T_{rc}), and melting temperature (T_m) of the ZIFs. The gray regions represent the second upscans.

is ca. 35 to 58 % lower than that of pure ZIF-zni(Zn) ($\Delta H_m = 11.9$ kJ mol^{-1}). Correspondingly, these recrystallized phases from the PSBM materials also exhibit substantially lower melting temperatures ($T_m = 570$ °C and 565 °C) compared to their pristine counterparts ($T_m \geq 581$ °C). The lower T_m and ΔH_m of the PSBM samples can be attributed to the presence of a considerable amount of residual amorphous content, a higher concentration of structural defects in the recrystallized phases, and the smaller particle sizes induced by PSBM (Figures S107–108).[51–53] Noteworthy, similar variations in the glass transition and recrystallization behavior are observed for the Co^{2+}-derivatives ZIF-4(Co) and ZIF-zni(Co), even though the ZIF-zni(Co) phases derived by recrystallization thermally decompose before they melt. (Figures 6d and S89).[34,54]

Excitingly, the PSBM samples of phase-pure ZIF-76 demonstrate clear T_g signals between 278 °C (15 min PSBM) and 347 °C (5 min PSBM) in the first DSC upscans (Figure 7). Similar to the behavior observed for the other ZIF glass formers discussed earlier, T_g converges to 357 °C in the second upscans due to thermal relaxation during the first heating-cooling cycle. Note that the glassy state of ZIF-76 is unattainable by the melt-quenching technique when the material is in phase-pure form because the ZIF-76 microcrystals reach their decomposition temperature (T_d) before

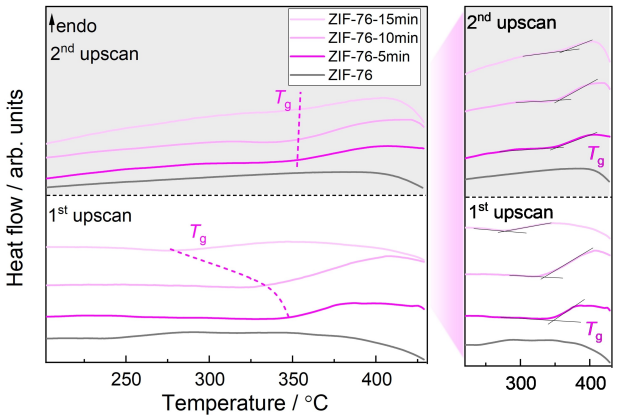

Figure 7. First and second upscans of DSC measurements of phase-pure ZIF-76 and the corresponding samples after 5, 10 and 15 min PSBM. The heating rate for all measurements was +10 °C min^{-1}. The graph on the right is used to highlight the glass transition signals.

they can melt (Figure S83).[36] Consequently, ZIF-76 can only be melted in a flux of a meltable ZIF, such as the chemically similar but topologically different ZIF-UC-5.[36,55–56] The inability of phase-pure ZIF-76 to melt can be attributed to its substantially higher porosity compared to

the ZIFs with **cag** or **zni** topology, which results in an increased activation energy for the dissociation of the metal-linker bond.[37] The strong densification experienced by ZIF-76 during PSBM (Figure 4a) appears to be the key to observing glassy behavior and forming a supercooled liquid state at elevated temperatures. This development is advantageous as it expands the range of chemical compositions available for ZIF glasses. Notably, the fraction of the bulky Clbim$^-$ linker in ZIF-76 accounts for approximately 50 %, whereas it is only around 20 % in ZIF-UC-5. This is relevant because the fraction of the bulky linker in ZIF glasses has been shown to influence important material properties, including the viscosity of the ZIF liquids and the gas sorption selectivity of the corresponding glasses.[17,39]

Inspired by the finding that the non-melting ZIF-76 can be transformed into a glass by PSBM, we embarked on an investigation into the thermal characteristics of ZIF-8, ZIF-70 and ZIF-Cu-1. We aimed to explore the possibility of observing glass transitions and attaining supercooled liquid states for these ZIFs following PSBM treatment as well. Crystalline ZIF-8 has already been investigated in terms of melting from an experimental and theoretical perspective,[4,37] while the thermal phase behavior of ZIF-70 and ZIF-Cu-1 is unexplored.

It is established that crystalline ZIF-8 is resistant to melting at elevated temperatures, which has been explained by the stronger Zn–N bond of the mim$^-$ linker compared to the non-substituted im$^-$ linker as well as the larger activation energy for Zn–N bond breaking originating from the large porosity of ZIF-8.[4,37,43] In agreement with these facts, none of the ball-milled ZIF-8 samples exhibits a calorimetric glass transition, although the amorphous ZIF materials possess rather high thermal stability (T_d > 486 °C) (Figures S85 and S90). It becomes evident that the densified amorphous ZIF-8 phases resulting from PSBM do not undergo the dynamic dissociation and association of Zn–N bonds, required for the transition from a vitrified glass to a supercooled liquid state. This observation underscores the critical role played by the non-substituted and smaller im$^-$ linker, which is an integral building block common to all reported glass-forming ZIFs.

ZIF-70 possesses a chemical composition with about 59 % of the small im$^-$ linker and about 41 % of the bulkier nim$^-$ linker. TG/DTA reveals that the crystalline ZIF-70 has a low T_d of 325 °C. In contrast to all the other ZIFs investigated in this work, ZIF-70 displays a strongly exothermic decomposition, which can be associated with the low thermal stability of the nim$^-$ linker. No melting signal can be observed in the DSC before the exothermic decomposition. The rather large fraction of the im$^-$ linkers, however, suggests that the material has the potential for glass formation by PSBM, akin to ZIF-76. Nevertheless, the amorphous ZIF-70 derivatives obtained through PSBM also exhibit a strongly exothermic decomposition starting already at around 300 °C (Figure S86). This low thermal stability of the amorphous ZIF-70 renders it incapable of showing a glass transition signal in DSC analysis, as T_g would be expected somewhere above 300 °C (Figure S91). Thus, the amorphized and densified ZIF-70 shows no glassy behavior, presumably due to its poor thermal stability.

To our knowledge, the thermal properties of the Cu^{2+}-based ZIF-Cu-1 have not yet been investigated, although the material with the **sod** topology was reported more than 20 years ago.[38] TG/DTA experiments reveal that crystalline ZIF-Cu-1 experiences a two-step decomposition process, with the first step starting at only 258 °C (Figure 8a). Hence, T_d of ZIF-Cu-1 is much lower compared to the previously discussed Zn^{2+}- and Co^{2+}-based ZIFs. The heat flow signature at the first decomposition step is strongly endothermic, and heating ZIF-Cu-1 just past the first decomposition step (i.e. to 270 °C) followed by cooling the material to room temperature results in a dark-colored, glassy material exhibiting a glass transition with a T_g of 172 °C upon reheating (Figure S99). The fact that the particles of the pristine microcrystalline ZIF-Cu-1 fuse to form a millimeter-sized glassy structure indicates that ZIF-Cu-1 melts and decomposes in parallel at around 258 °C. Since the weight-loss is about 22 % for the first decomposition step,

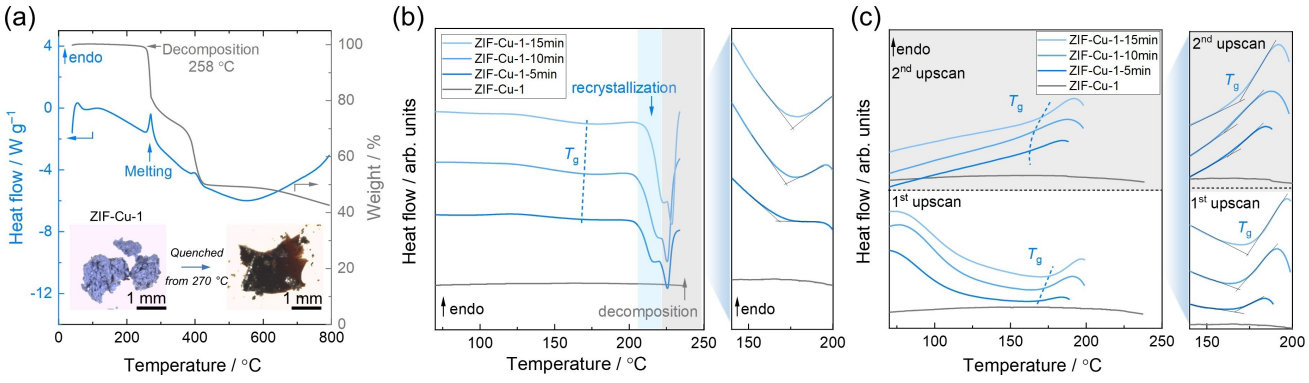

Figure 8. (a) TG/DTA data of ZIF-Cu-1. The inset is microscopic images of the neat ZIF-Cu-1 microcrystalline powder and the glassy phase derived by heating ZIF-Cu-1 to 270 °C under N_2 atmosphere (i.e. to the offset of the endothermic DTA signal) followed by cooling to room temperature. (b) DSC measurements of ZIF-Cu-1 and its PSBM derivatives recorded to a maximum temperature of 235 °C. (c) Cyclic DSC scans of ZIF-Cu-1 and its PSBM derivatives. To avoid recrystallization of the PSBM samples, the first upscan was heated to only 190 or 200 °C. The heating rate for all measurements was +10 °C min^{-1}. The zoom on the right in panels (b) and (c) is to highlight the glass transition signals.

the glassy phase of ZIF-Cu-1 derived by melt-quenching suffers from severe decomposition. Excitingly, the ZIF-Cu-1 samples amorphized by PSBM display glass transition temperatures between 166 °C and 170 °C in DSC experiments, classifying them as MIGs. In contrast to the Zn- and Co-based MIGs, the ZIF-Cu-1 samples processed for 5–15 min exhibit a slight increase in T_g with longer PSBM durations. This distinctive behavior could be due to the unique coordination chemistry of Cu^{2+} (Figure 5). Upon further heating, the MIGs recrystallize to the original ZIF-Cu-1 phase with **sod** topology, demonstrated by exothermic signals with an onset around 202 °C (Figure 8b) and the reappearance of characteristic diffraction peaks in the XRPD patterns (Figure S20). The recrystallization is followed by thermal decomposition around 220 °C. However, if the MIGs are only heated to 200 °C, recrystallization does not occur, and glass transitions are again observed in the second DSC upscans (Figure 8c). Importantly, the MIGs of ZIF-Cu-1 are the first Cu^{2+}-based ZIF glasses, enhancing the compositional variety of the ZIF glass family beyond the materials with Zn^{2+}, Co^{2+} and Fe^{2+} metal centers[57] reported so far. Given the unique catalytic, electronic and redox properties of Cu^{2+}-based MOFs,[58–60] the finding that PSBM gives access to Cu^{2+}-based MOF glasses significantly expands the range of potential applications of this family of materials.

Among the known ZIF glass formers of the composition $M(im)_2$, with M^{2+}=Zn^{2+} (ZIF-4), Co^{2+} (ZIF-4), Fe^{2+} (MUV-24) and Cu^{2+} (ZIF-Cu-1), the Cu-derivative is unique. The metastable ZIF-4 (**cag** topology) and MUV-24 (*lla1* topology) recrystallize to polymorphs with **zni** topology upon thermal treatment, and the $M(im)_2$ phases with **zni** topology melt (decompose in the case of Co^{2+}) at temperatures between 482 and 590 °C.[57] The liquids of $Zn(im)_2$ and $Fe(im)_2$ can be quenched to room temperature to derive their glasses with glass transition temperatures of 292 °C (Zn^{2+}) or 190 °C (Fe^{2+}). ZIF-Cu-1 possesses the **sod** topology, which is already quite dense because of the unique flattened tetrahedral coordination geometry of the Cu^{2+} ion (Figure 2). A solid-solid transition to a polymorph with **zni** topology is not observed for $Cu(im)_2$, likely because the **zni** topology cannot be realized with the flattened tetrahedral Cu^{2+} geometry. Instead, ZIF-Cu-1 melts at a much lower temperature (~260 °C) and decomposes in parallel. Nevertheless, employing the PSBM technique, a non-decomposed, glassy form of ZIF-Cu-1 can be obtained, exhibiting a T_g of ~166 °C. Therefore, the T_g, T_m and T_d of ZIF-Cu-1 are the lowest in the $M(im)_2$ series. This indicates a greater lability of the Cu–N bond compared to the bonds involving the other M^{2+} ions.

Conclusion

In our study, we investigated the amorphization and glass formation of twelve distinct ZIFs featuring a range of imidazolate-type linkers and metal ions (Zn^{2+}, Co^{2+} and Cu^{2+}) through solvent-free PSBM. We observed that ZIFs capable of melting and forming melt-quenched glasses also vitrify via PSBM. Conversely, ZIFs that decompose thermally before melting exhibit varied responses to ball milling; some display glass-like properties, while others do not. The absence of glassy behavior in ZIF-8 and ZIF-70 can be attributed to the exceptionally strong Zn–N bond with the mim^- linker in ZIF-8 and the very limited thermal stability of the nim^- linker in ZIF-70. In the case of the non-melting ZIF-76, vitrification through PSBM is achievable since the imidazolate-type linkers in this material have adequate thermal stability and sufficient Zn–N bond lability. The significance of PSBM in forming ZIF glasses is particularly evident in the case of ZIF-Cu-1. The lower thermal stability of ZIF-Cu-1 likely originates from the labile Cu–N bonds and the redox activity of the Cu^{2+} centers, leading to simultaneous melting and thermal decomposition of the crystalline ZIF-Cu-1 phase. However, amorphization by PSBM enables the attainment of a glassy state in ZIF-Cu-1 while maintaining material integrity, marking the creation of the first Cu^{2+}-based ZIF glass.

Our research underscores the vast potential of PSBM in developing new glassy ZIFs. While the small particle size of the PSBM-derived glasses may limit their direct application, the process of sintering or remelting by heating the materials above their T_g facilitates particle fusion and enables the formation of bulk glasses.[61–62] Future studies should explore the applicability of PSBM for producing glassy MOFs utilizing alternative linker chemistries, such as dicarboxylates.[63–64] This expansion could be pivotal in broadening the scope of MOF glasses, traditionally constrained by the necessity for MOFs to be meltable—a characteristic that only a limited number of MOFs exhibit. Thus, we envisage that several non-meltable ZIFs and other MOFs can also be vitrified by PSBM. Moreover, creating MOF glasses through ball-milling at room temperature may not only be more energy-efficient[31] but also enable the integration of thermally sensitive materials, such as organic or organometallic molecules, into versatile MOF glass composites.[65] This approach broadens the spectrum of potential applications, paving the way for developing multifunctional MOF glass composites, thereby venturing into more diverse application fields.

Supporting Information

Details on materials synthesis, further X-ray powder diffraction (XRPD), synchrotron radiation variable temperature XRPD (VT-XRPD), X-ray total scattering, simultaneous thermogravimetric analysis (TGA) and differential scanning calorimetry (DSC), FTIR and ^{1}H NMR spectroscopy, scanning electron microscopy (SEM), optical microscopy and further gas physisorption data and analytical procedures.

Acknowledgements

The Deutsche Forschungsgemeinschaft, DFG, (project 447344931, HE 7628/7-1) is acknowledged for funding.

W.L.X acknowledges the China Scholarship Council (CSC No. 202008110211). J.-B.W. acknowledges the Fonds der Chemischen Industrie for a Kekulè Fellowship. The authors thank DELTA Dortmund for the allocation of beamtime at beamline BL9 and Dr. Christian Sternemann and Dr. Michael Paulus for their help with the variable temperature XRPD experiments. We acknowledge DESY (Hamburg, Germany), a member of the Helmholtz Association HGF, for the provision of experimental facilities. X-ray total scattering of this research was carried out at PETRA III on beamline P02.1 (proposal I-20210316 and rapid access 20010266). We thank Pascal Kolodzeiski, Dr. Jianbo Song, Dr. Athanasios Koutsianos, Dr. Roman Pallach, and Dr. Louis Frentzel-Beyme for their help with the measurement and analysis of X-ray total scattering data. We thank Dr. Martin Etter for measuring our samples remotely during the Rapid Access beamtime (20010266). Guoqiang Li is acknowledged for helping with the synthesis of phase-pure ZIF-76. Volker Brandt is acknowledged for the collection of SEM images. Open Access funding enabled and organized by Projekt DEAL.

Conflict of Interest

The authors declare no competing financial interest.

Data Availability Statement

The data that support the findings of this study are available in the supplementary material of this article.

Keywords: Metal–organic frameworks · Mechanical chemistry · Phase transition · Glass formation · Amorphization

[1] H. Furukawa, K. E. Cordova, M. O'Keeffe, O. M. Yaghi, *Science* **2013**, *341*, 1230444.
[2] P. Z. Moghadam, A. Li, X. W. Liu, R. Bueno-Perez, S. D. Wang, S. B. Wiggin, P. A. Wood, D. Fairen-Jimenez, *Chem. Sci.* **2020**, *11*, 8373–8387.
[3] R. Gaillac, P. Pullumbi, K. A. Beyer, K. W. Chapman, D. A. Keen, T. D. Bennett, F. X. Coudert, *Nat. Mater.* **2017**, *16*, 1149–1154.
[4] T. D. Bennett, J. C. Tan, Y. Yue, E. Baxter, C. Ducati, N. J. Terrill, H. H. Yeung, Z. Zhou, W. Chen, S. Henke, A. K. Cheetham, G. N. Greaves, *Nat. Commun.* **2015**, *6*, 8079.
[5] N. Ma, S. Horike, *Chem. Rev.* **2022**, *122*, 4163–4203.
[6] S. Horike, S. S. Nagarkar, T. Ogawa, S. Kitagawa, *Angew. Chem. Int. Ed.* **2020**, *59*, 6652–6664.
[7] Y. Wang, H. Jin, Q. Ma, K. Mo, H. Mao, A. Feldhoff, X. Cao, Y. Li, F. Pan, Z. Jiang, *Angew. Chem. Int. Ed.* **2020**, *59*, 4365–4369.
[8] N. Ma, S. Kosasang, A. Yoshida, S. Horike, *Chem. Sci.* **2021**, *12*, 5818–5824.
[9] G. Jiang, C. Qu, F. Xu, E. Zhang, Q. Lu, X. Cai, S. Hausdorf, H. Wang, S. Kaskel, *Adv. Funct. Mater.* **2021**, *31*, 2104300.
[10] J. Hou, P. Chen, A. Shukla, A. Krajnc, T. Wang, X. Li, R. Doasa, H. G. Tizei Luiz, B. Chan, N. Johnstone Duncan, R. Lin, U. Schülli Tobias, I. Martens, D. Appadoo, S. Ari Mark, Z. Wang, T. Wei, S.-C. Lo, M. Lu, S. Li, B. Namdas Ebinazar, G. Mali, K. Cheetham Anthony, M. Collins Sean, V. Chen, L. Wang, D. Bennett Thomas, *Science* **2021**, *374*, 621–625.
[11] H. Tao, T. D. Bennett, Y. Yue, *Adv. Mater.* **2017**, *29*.
[12] R. Banerjee, A. Phan, B. Wang, C. Knobler, H. Furukawa, M. O'Keeffe, M. Yaghi Omar, *Science* **2008**, *319*, 939–943.
[13] J. Song, L. Frentzel-Beyme, R. Pallach, P. Kolodzeiski, A. Koutsianos, W.-L. Xue, R. Schmid, S. Henke, *J. Am. Chem. Soc.* **2023**, *145*, 9273–9284.
[14] C. Healy, K. M. Patil, B. H. Wilson, L. Hermanspahn, N. C. Harvey-Reid, B. I. Howard, C. Kleinjan, J. Kolien, F. Payet, S. G. Telfer, P. E. Kruger, T. D. Bennett, *Coord. Chem. Rev.* **2020**, *419*, 213388.
[15] R. Banerjee, H. Furukawa, D. Britt, C. Knobler, M. O'Keeffe, O. M. Yaghi, *J. Am. Chem. Soc.* **2009**, *131*, 3875–3877.
[16] T. D. Bennett, Y. Yue, P. Li, A. Qiao, H. Tao, N. G. Greaves, T. Richards, G. I. Lampronti, S. A. T. Redfern, F. Blanc, O. K. Farha, J. T. Hupp, A. K. Cheetham, D. A. Keen, *J. Am. Chem. Soc.* **2016**, *138*, 3484–3492.
[17] L. Frentzel-Beyme, P. Kolodzeiski, J.-B. Weiß, A. Schneemann, S. Henke, *Nat. Commun.* **2022**, *13*, 7750.
[18] S. Głowniak, B. Szczęśniak, J. Choma, M. Jaroniec, *Mater. Today.* **2021**, *46*, 109–124.
[19] P. J. Beldon, L. Fábián, R. S. Stein, A. Thirumurugan, A. K. Cheetham, T. Friščić, *Angew. Chem. Int. Ed.* **2010**, *49*, 9640–9643.
[20] W. Xu, H. Chen, K. Jie, Z. Yang, T. Li, S. Dai, *Angew. Chem. Int. Ed.* **2019**, *58*, 5018–5022.
[21] T. Panda, S. Horike, K. Hagi, N. Ogiwara, K. Kadota, T. Itakura, M. Tsujimoto, S. Kitagawa, *Angew. Chem. Int. Ed.* **2017**, *56*, 2413–2417.
[22] N. Ma, R. Ohtani, H. M. Le, S. S. Sørensen, R. Ishikawa, S. Kawata, S. Bureekaew, S. Kosasang, Y. Kawazoe, K. Ohara, M. M. Smedskjaer, S. Horike, *Nat. Commun.* **2022**, *13*, 4023.
[23] Y. Ohara, A. Hinokimoto, W. Chen, T. Kitao, Y. Nishiyama, Y.-l. Hong, S. Kitagawa, S. Horike, *Chem. Commun.* **2018**, *54*, 6859–6862.
[24] Z. Yin, Y.-B. Zhang, H.-B. Yu, M.-H. Zeng, *Sci. Bull.* **2020**, *65*, 1432–1435.
[25] R. N. Widmer, G. I. Lampronti, S. Anzellini, R. Gaillac, S. Farsang, C. Zhou, A. M. Belenguer, C. W. Wilson, H. Palmer, A. K. Kleppe, M. T. Wharmby, X. Yu, S. M. Cohen, S. G. Telfer, S. A. T. Redfern, F. X. Coudert, S. G. MacLeod, T. D. Bennett, *Nat. Mater.* **2019**, *18*, 370–376.
[26] S.-X. Peng, Z. Yin, T. Zhang, Q. Yang, H.-B. Yu, M.-H. Zeng, *J. Chem. Phys.* **2022**, *157*, 104501.
[27] T. D. Bennett, S. Cao, J. C. Tan, D. A. Keen, E. G. Bithell, P. J. Beldon, T. Friscic, A. K. Cheetham, *J. Am. Chem. Soc.* **2011**, *133*, 14546–14549.
[28] E. F. Baxter, T. D. Bennett, A. B. Cairns, N. J. Brownbill, A. L. Goodwin, D. A. Keen, P. A. Chater, F. Blanc, A. K. Cheetham, *Dalton Trans.* **2016**, *45*, 4258–4268.
[29] T. D. Bennett, P. J. Saines, D. A. Keen, J.-C. Tan, A. K. Cheetham, *Chem. Eur. J.* **2013**, *19*, 7049–7055.
[30] S. Cao, T. D. Bennett, D. A. Keen, A. L. Goodwin, A. K. Cheetham, *Chem. Commun.* **2012**, *48*, 7805–7807.
[31] M. F. Thorne, M. L. R. Gómez, A. M. Bumstead, S. Li, T. D. Bennett, *Green Chem.* **2020**, *22*, 2505–2512.
[32] R. Lin, X. Li, A. Krajnc, Z. Li, M. Li, W. Wang, L. Zhuang, S. Smart, Z. Zhu, D. Appadoo, J. R. Harmer, Z. Wang, A. G. Buzanich, S. Beyer, L. Wang, G. Mali, T. D. Bennett, V. Chen, J. Hou, *Angew. Chem. Int. Ed.* **2022**, *61*, e202112880.
[33] M. F. Thorne, A. F. Sapnik, L. N. McHugh, A. M. Bumstead, C. Castillo-Blas, D. S. Keeble, M. Diaz Lopez, P. A. Chater, D. A. Keen, T. D. Bennett, *Chem. Commun.* **2021**, *57*, 9272–9275.

[34] L. Frentzel-Beyme, M. Kloß, R. Pallach, S. Salamon, H. Moldenhauer, J. Landers, H. Wende, J. Debus, S. Henke, *J. Mater. Chem. A* **2019**, *7*, 985–990.
[35] J. Hou, M. L. Ríos Gómez, A. Krajnc, A. McCaul, S. Li, A. M. Bumstead, A. F. Sapnik, Z. Deng, R. Lin, P. A. Chater, D. S. Keeble, D. A. Keen, D. Appadoo, B. Chan, V. Chen, G. Mali, T. D. Bennett, *J. Am. Chem. Soc.* **2020**, *142*, 3880–3890.
[36] A. M. Bumstead, M. L. Ríos Gómez, M. F. Thorne, A. F. Sapnik, L. Longley, J. M. Tuffnell, D. S. Keeble, D. A. Keen, T. D. Bennett, *CrystEngComm* **2020**, *22*, 3627–3637.
[37] R. Gaillac, P. Pullumbi, F.-X. Coudert, *J. Phys. Chem. C* **2018**, *122*, 6730–6736.
[38] N. Masciocchi, S. Bruni, E. Cariati, F. Cariati, S. Galli, A. Sironi, *Inorg. Chem.* **2001**, *40*, 5897–5905.
[39] L. Frentzel-Beyme, M. Kloss, P. Kolodzeiski, R. Pallach, S. Henke, *J. Am. Chem. Soc.* **2019**, *141*, 12362–12371.
[40] A. M. Bumstead, M. F. Thorne, A. F. Sapnik, C. Castillo-Blas, G. I. Lampronti, T. D. Bennett, *Dalton Trans.* **2022**, *51*, 13636–13645.
[41] J. C. Tan, T. D. Bennett, A. K. Cheetham, *Proc. Natl. Acad. Sci. USA* **2010**, *107*, 9938–9943.
[42] T. D. Bennett, A. L. Goodwin, M. T. Dove, D. A. Keen, M. G. Tucker, E. R. Barney, A. K. Soper, E. G. Bithell, J.-C. Tan, A. K. Cheetham, *Phys. Rev. Lett.* **2010**, *104*, 115503.
[43] W.-L. Xue, P. Kolodzeiski, H. Aucharova, S. Vasa, A. Koutsianos, R. Pallach, J. Song, L. Frentzel-Beyme, R. Linser, S. Henke, *Nat. Commun.* **2024**, *15*, 4420.
[44] J. Song, R. Pallach, L. Frentzel-Beyme, P. Kolodzeiski, G. Kieslich, P. Vervoorts, C. L. Hobday, S. Henke, *Angew. Chem. Int. Ed.* **2022**, *61*, e202117565.
[45] S.-i. Noro, X. Zheng, A. Wang, K. Suzuki, S. Kosasang, S. Horike, D. Padovan, K. Nakajima, H. Sato, K. Takahashi, T. Nakamura, *Inorg. Chem.* **2022**, *61*, 3379–3386.
[46] L. Yang, D. R. Powell, R. P. Houser, *Dalton Trans.* **2007**, 955–964.
[47] E. D. Zanotto, J. C. Mauro, *J. Non-Cryst. Solids* **2017**, *471*, 490–495.
[48] A. A. L. Michalchuk, F. Emmerling, *Angew. Chem. Int. Ed.* **2022**, *61*, e202117270.
[49] W. Wang, M. Chai, M. Y. Bin Zulkifli, K. Xu, Y. Chen, L. Wang, V. Chen, J. Hou, *Mol. Syst. Des. Eng.* **2023**, *8*, 560–579.
[50] C. Castillo-Blas, A. M. Chester, R. P. Cosquer, A. F. Sapnik, L. Corti, R. Sajzew, B. Poletto-Rodrigues, G. P. Robertson, D. J. M. Irving, L. N. McHugh, L. Wondraczek, F. Blanc, D. A. Keen, T. D. Bennett, *J. Am. Chem. Soc.* **2023**, *145*, 22913–22924.
[51] C. Suryanarayana, *Prog. Mater. Sci.* **2001**, *46*, 1–184.
[52] H. Jiang, K.-s. Moon, H. Dong, F. Hua, C. P. Wong, *Chem. Phys. Lett.* **2006**, *429*, 492–496.
[53] A. van Teijlingen, S. A. Davis, S. R. Hall, *Nanoscale Adv.* **2020**, *2*, 2347–2351.
[54] K. Li, H. Xiao, J. He, H. Jiang, *NANO* **2018**, *13*, 1850025.
[55] V. Nozari, O. Smirnova, J. M. Tuffnell, A. Knebel, T. D. Bennett, L. Wondraczek, *Adv. Mater. Technol.* **2022**, *7*, 2200343.
[56] C. Zhou, L. Longley, A. Krajnc, G. J. Smales, A. Qiao, I. Erucar, C. M. Doherty, A. W. Thornton, A. J. Hill, C. W. Ashling, O. T. Qazvini, S. J. Lee, P. A. Chater, N. J. Terrill, A. J. Smith, Y. Yue, G. Mali, D. A. Keen, S. G. Telfer, T. D. Bennett, *Nat. Commun.* **2018**, *9*, 5042.
[57] L. León-Alcaide, R. S. Christensen, D. A. Keen, J. L. Jordá, I. Brotons-Alcázar, A. Forment-Aliaga, G. Mínguez Espallargas, *J. Am. Chem. Soc.* **2023**, *145*, 11258–11264.
[58] I. Luz, F. X. Llabrés i Xamena, A. Corma, *J. Catal.* **2010**, *276*, 134–140.
[59] Y. Ma, X. Han, S. Xu, Z. Wang, W. Li, I. da Silva, S. Chansai, D. Lee, Y. Zou, M. Nikiel, P. Manuel, A. M. Sheveleva, F. Tuna, E. J. L. McInnes, Y. Cheng, S. Rudić, A. J. Ramirez-Cuesta, S. J. Haigh, C. Hardacre, M. Schröder, S. Yang, *J. Am. Chem. Soc.* **2021**, *143*, 10977–10985.
[60] J. Park, A. C. Hinckley, Z. Huang, D. Feng, A. A. Yakovenko, M. Lee, S. Chen, X. Zou, Z. Bao, *J. Am. Chem. Soc.* **2018**, *140*, 14533–14537.
[61] X. Li, R. Lin, J. Hou, L. Wang, *Cell Rep. Phys. Sci.* **2022**, *3*, 100932.
[62] S. Li, R. Limbach, L. Longley, A. A. Shirzadi, J. C. Walmsley, D. N. Johnstone, P. A. Midgley, L. Wondraczek, T. D. Bennett, *J. Am. Chem. Soc.* **2019**, *141*, 1027–1034.
[63] M. Kim, H.-S. Lee, D.-H. Seo, S. J. Cho, E.-c. Jeon, H. R. Moon, *Nat. Commun.* **2024**, *15*, 1174.
[64] W.-L. Xue, G.-Q. Li, H. Chen, Y.-C. Han, L. Feng, L. Wang, X.-L. Gu, S.-Y. Hu, Y.-H. Deng, L. Tan, M. T. Dove, W. Li, J. Zhang, H. Dong, Z. Chen, W.-H. Deng, G. Xu, G. Wang, C.-Q. Wan, *Nat. Commun.* **2024**, *15*, 2040.
[65] R. Lin, M. Chai, Y. Zhou, V. Chen, T. D. Bennett, J. Hou, *Chem. Soc. Rev.* **2023**, *52*, 4149–4172.

Manuscript received: March 18, 2024
Accepted manuscript online: June 14, 2024
Version of record online: August 14, 2024